APS physics

CHORUS

This is the accepted manuscript made available via CHORUS. The article has been published as:

Controlling rare-earth ions in a nanophotonic resonator using the ac Stark shift

John G. Bartholomew, Tian Zhong, Jonathan M. Kindem, Raymond Lopez-Rios, Jake Rochman, Ioana Craiciu, Evan Miyazono, and Andrei Faraon

Phys. Rev. A **97**, 063854 — Published 28 June 2018

DOI: 10.1103/PhysRevA.97.063854

Controlling rare-earth ions in a nanophotonic resonator using the ac Stark shift

John G. Bartholomew,[1,2] Tian Zhong,[1,2,3] Jonathan M. Kindem,[1,2] Raymond Lopez-Rios,[1,2] Jake Rochman,[1,2] Ioana Craiciu,[1,2] Evan Miyazono,[1,2] and Andrei Faraon[1,2,*]

[1]*Kavli Nanoscience Institute and Thomas J. Watson, Sr., Laboratory of Applied Physics, California Institute of Technology, Pasadena, California 91125, USA.*
[2]*Institute for Quantum Information and Matter, California Institute of Technology, Pasadena, California 91125, USA.*
[3]*Institute of Molecular Engineering, University of Chicago, Chicago, Illinois 60637, USA*

(Dated: June 11, 2018)

On-chip nanophotonic cavities will advance quantum information science and measurement because they enable efficient interaction between photons and long-lived solid-state spins, such as those associated with rare-earth ions in crystals. The enhanced photon-ion interaction creates new opportunities for all-optical control using the ac Stark shift. Toward this end, we characterize the ac Stark interaction between off-resonant optical fields and Nd^{3+}-ion dopants in a photonic crystal resonator fabricated from yttrium orthovanadate (YVO_4). Using photon echo techniques, at a detuning of 160 MHz we measure a maximum ac Stark shift of $2\pi \times 12.3$ MHz per intra-cavity photon, which is large compared to both the homogeneous linewidth (Γ_h= 84 kHz) and characteristic width of isolated spectral features created through optical pumping ($\Gamma_f \approx 3$ MHz). The photon-ion interaction strength in the device is sufficiently large to control the frequency and phase of the ions for quantum information processing applications. In particular, we discuss and assess the use of the cavity enhanced ac Stark shift to realize all-optical quantum memory and detection protocols. Our results establish the ac Stark shift as a powerful added control in rare-earth ion quantum technologies.

I. INTRODUCTION

Efficient interfaces between photons and spins in solids are one foundation for building integrable and scalable quantum technologies for computing, communication, and metrology. One promising system for realizing photon-spin interfaces to create, control, and store quantum states is crystals containing rare-earth ions (REIs). Experiments in REI crystals have demonstrated entangled photon-pair generation [1–3], quantum memories for light [4–6], and qubit operations [7]. These results, combined with some of the longest optical and spin coherence times in the solid state [8–11] establish the future potential of REI quantum technologies.

In most cases, quantum optical protocols performed in REI materials rely on large ensembles (10^9 ions) to compensate for the weakly allowed $4f \leftrightarrow 4f$ optical transitions [12]. Although this approach has proved effective, the use of large ensembles in doped crystals sets a macroscopic lower bound on the device size. This is because increasing the spectral-spatial density of REI dopants increases ion-ion interactions that cause added inhomogeneity and decoherence. The size restriction imposed by the use of large ensembles places limits on the integration and scalability of the REI platform. Thus, there is significant impetus to develop other methods to increase photon-ion interactions [13–17]. One solution is to fabricate photonic crystal resonators directly in REI crystals [15, 18–21]. A large increase in photon-ion coupling is achieved through cavity enhancement of the optical transition [22] and strong mode confinement [14, 23–26]. Thus, these photonic crystal resonators are suited to harnessing phenomena that are more commonly associated with systems with strong optical transitions, such as the ac Stark shift (ACSS). Although the ACSS has been investigated in REI crystals [27–29], the interaction resulted from $\approx 10^8$ photons interacting with $\approx 10^8$ ions.

In this work we characterize the ACSS in an on-chip nanophotonic resonator, where the strength of the ACSS is sufficiently large to measure the interaction between a single photon and approximately 4×10^3 Nd^{3+}-ions. The ACSS was probed using a photon echo technique, which allowed the measurement of the maximum ACSS and the inhomogeneity of the interaction in the cavity. These measurements are then used to assess the ACSS as a tool for REI quantum optics. In particular, we discuss using the large ACSS to realize all-optical quantum memories based on the hybrid photon echo rephasing (HYPER) protocol [30] and the atomic frequency comb (AFC) [31], and cross phase modulation using the protocol suggested in Reference 29. Our study demonstrates that the enhanced photon-ion interactions resulting from coupling of REIs to photonic crystal resonators offer new avenues for quantum technologies in these materials.

II. AC STARK SHIFT CHARACTERIZATION

A. Summary of device, apparatus, and calibration

The material chosen for this work was YVO_4 doped with a Nd^{3+}-ion impurity at a nominal level of 50 ppm (Gamdan Optics). We use the 879.9 nm transition between the lowest crystal field components of the $^4I_{9/2}$ and

* Email address: faraon@caltech.edu

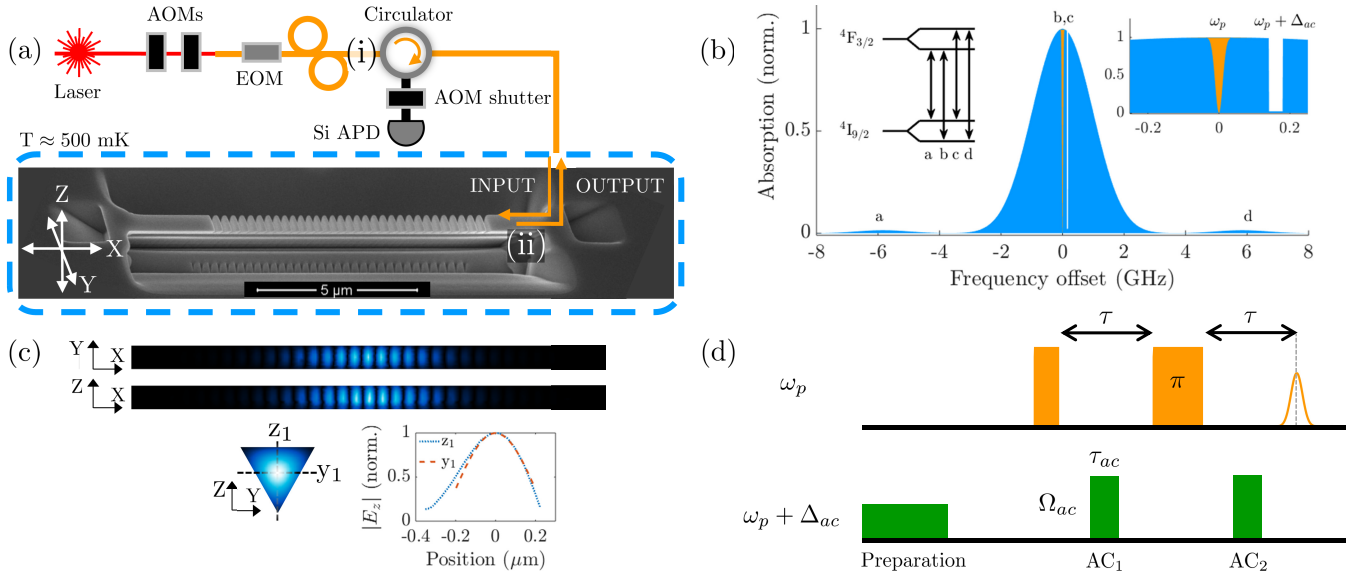

FIG. 1. (a) Schematic of the experimental apparatus. A cw Ti:Sapphire laser is gated by two acousto-optic modulators (AOMs) and an electro-optic modulator (EOM) to create pulses that are coupled into the nanophotonic device, which is maintained at approximately 500 mK in a ^{3}He refrigerator. The photonic crystal cavity was fabricated on the surface of a Nd^{3+}:YVO_4 substrate and is one-sided to allow measurements to be performed in the reflection mode. (b) The optical absorption of the $^4I_{9/2}(Z1) \leftrightarrow {}^4F_{3/2}(Y1)$ transition in Nd^{3+}:YVO_4 modeled from the spin Hamiltonian, which shows the spectral subset of ions that contribute to the photon echo signal (at frequency ω_p), and the transmission trench prepared for the ACSS pulses (at frequency $\omega_p + \Delta_{ac}$). The inset on the left shows the energy level structure of the transition, and the inset on the right shows the spectral region of interest in greater detail. (c) Cross-sections of $|E_z|$ in the cavity, which illustrate the spatial inhomogeneity of the cavity field. The inset shows the variation of $|E_z|$ along lines y_1 and z_1, indicating the smaller variation of the field along the y-axis. (d) An example pulse sequence for the photon echo measurements used in this work.

$^4F_{3/2}$ multiplets. Both these levels are Kramers doublets, the degeneracy of which is lifted in an applied magnetic field resulting in four optical transitions (see Figure 1(b)). This transition has been characterized previously [31–33] and shown to possess narrow inhomogeneous linewidths, and the largest documented optical dipole moment for REI transitions suitable for quantum memory applications [34]. Furthermore, optical pumping of Nd^{3+}:YVO_4 allows the electron spin to be highly polarized [21, 31, 33], because of long lived spin states. Notably, the Nd^{3+} site has D_{2d} symmetry and hence, has a vanishing dc Stark shift. As a result, despite the high absorption possible in this material, its use in quantum memory applications has been limited because electric fields cannot be used to control the ions.

A one-sided photonic crystal cavity was milled into the Nd^{3+}:YVO_4 surface perpendicular to the crystal c-axis using a focused ion beam [15, 18, 21]. To couple the TM mode illustrated in Figure 1(c) to the Nd^{3+} optical transition, the cavity is frequency tuned through nitrogen gas condensation. The device was cooled to approximately 500 mK in a ^{3}He cryostat to reduce transition broadening due to phonon interactions. In addition, a constant magnetic field of approximately 340 mT was applied at a small angle from the YVO_4 c-axis to reduce broadening from Nd^{3+}-Nd^{3+} magnetic dipole interactions. Further details about the cavity and the experimental setup are provided in Appendix A.

The ACSS is characterized through the study of two pulse photon echoes [27, 28], which were detected by photon counting with a silicon avalanche photodiode (APD). The two pulse echo sequence was augmented by additional off-resonant ACSS pulses (AC1 and AC2) before and after the inverting π-pulse (see Figure 1(d), and the insets of Figure 3). To reduce any resonant interactions between the ions and the ACSS pulses, spectral trenches were prepared at the ACSS frequencies prior to the sequence by optically pumping to the other electron spin level (see Figure 1(b)). During the off-resonant ACSS pulses of length τ_{ac}, the optical transition of each ion is frequency shifted by

$$\delta_{ac}(\boldsymbol{r}) \approx \Omega_{ac}(\boldsymbol{r})^2/(2\Delta_{ac}) \ , \qquad (1)$$

where $\Omega_{ac}(\boldsymbol{r})$ is the Rabi frequency at spatial position $\boldsymbol{r}$, and Δ_{ac} is the detuning of the ACSS pulse from the echo input pulse. The resulting phase accumulated by each ion is

$$\phi(\boldsymbol{r}) = \delta_{ac}(\boldsymbol{r})\tau_{ac} \ , \qquad (2)$$

which is governed by the field amplitude of the cavity mode at the ion's spatial location. Because there is no correlation between an ion's resonant frequency and its

position in the cavity, the application of an ACSS pulse results in an inhomogeneous phase shift across the ensemble. The inhomogeneity resulting from the ACSS pulse cannot be rephased by the optical π pulse, which leads to a decrease of the photon echo intensity. As $\phi(\boldsymbol{r})$ increases the echo intensity can oscillate because subensembles with phase shifts that differ by multiples of 2π (π) sum to increase (decrease) the coherent emission, but this modulation is strongly damped due to the increasing inhomogeneity [30]. It is possible, however, to rephase this ACSS-induced inhomogeneity through the application of additional ACSS pulses.

The average cavity photon population $\langle n\rangle$ was calculated from the pulse input power using the known losses in the apparatus and the measured cavity parameters. For all measurements the cw power of the laser was recorded at (i) before fiber-coupling to the circulator (see Figure 1(a)). The relative intensity of pulses at (ii), in the device waveguide (see Figure 1(a)), compared to the cw light at (i) was 0.011, which included loss due to the finite rise time of the AOMs for 20 ns pulses (23.5% transmission), the circulator loss (49.2% transmission), fiber coupling and splicing losses (35% transmission), and the fiber to waveguide coupling (27% transmission).

The average steady state photon number in the cavity $\langle n\rangle$ given an average photon number rate in the waveguide $|a_{in}|^2$ is given by

$$\langle n\rangle = \frac{\kappa_{\text{in}}}{(\kappa/2)^2 + \Delta_{\text{cav}}^2}|a_{in}|^2 \ , \tag{3}$$

where κ_{in} and κ are the energy decay rates through the input coupler and entire cavity, respectively, and Δ_{cav} is the detuning between the cavity and the ion ensemble. For the ACSS measurements $\kappa_{\text{in}} = 2\pi \times 45$ GHz, $\kappa = 2\pi \times 118$ GHz, and $\Delta_{\text{cav}} = -2\pi \times 27$ GHz.

To calibrate the average Rabi frequency $\bar{\Omega}$ for a given $\langle n\rangle$, two-pulse photon echoes were used to observe Rabi flopping of the ensemble. Figure 2 shows indicative data where the echo intensity was monitored as a function of pulse intensity $\langle n\rangle$ and rephasing pulse duration. Sustained Rabi flopping is not observed for two reasons. First, the inhomogeneity in the Rabi frequency dampens out the coherent oscillations. Second, it is likely that at the higher power levels, longer pulses lead to local heating in the cavity leading to an increased rate of decoherence. This explains the more definitive Rabi flopping curves observed for intensities $\langle n\rangle < 0.34$.

For the ACSS measurements a Rabi frequency of $\bar{\Omega} = 2\pi \times 25$ MHz was chosen for the input and rephasing pulses, which corresponded to $\langle n\rangle = 0.53$ (a cw laser power at (i) of 6.5 μW).

B. ac Stark shift measurement

Figure 3 shows the normalized intensity of the photon echo for sequences that vary (a) the average Rabi frequency of the ACSS pulses $\bar{\Omega}_{ac}$, (b) their duration, and

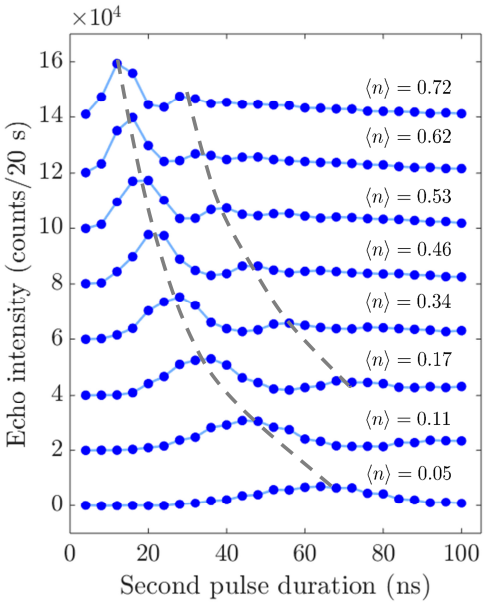

FIG. 2. Two pulse photon echo intensity as a function of the length of the second pulse for a given pulse intensity $\langle n\rangle$. Each data set is offset by 2×10^4 counts for clarity. The dashed gray lines are a guide to the eye for the first and second maxima of the Rabi flopping.

(c) their relative frequency detuning. The data highlights the ability to control the coherent emission intensity by manipulating the relative phase evolution throughout the ensemble using the ACSS. In the case where only a single ACSS pulse is applied (circles in Figure 3), the ACSS-induced inhomogeneity cannot be rephased and the echo is attenuated. The phase accumulated due to AC1 can be balanced through the application of an identical ACSS pulse after the π-pulse, which in principle can restore the echo to full intensity. Figure 3(a) (squares) demonstrates where this has been partially achieved through the application of AC2. On average the echo is restored to greater than 75% of the unperturbed echo intensity [35]. The incomplete recovery is likely to be dominated by imperfections in balancing the phase evolution from pulses AC1 and AC2, largely because of limitations in the timing resolution and intensity control of the applied ACSS pulses in our experimental setup (see Section II C). Importantly, the restoration of the echo is evidence that the attenuation is caused by the ACSS interaction rather than by other dephasing processes such as instantaneous spectral diffusion, or device heating.

The echo intensity was simulated using the cavity Maxwell-Bloch equations under the assumption of a uniform distribution of ions within the mode profile of the cavity (see Appendix B). Figure 3 shows normalized echo intensities from both a simplified analytical model (dashed line) and a numerical simulation (solid line). The analytical model assumed a two-dimensional Gaussian distribution [28] for the cavity mode profile. This is a

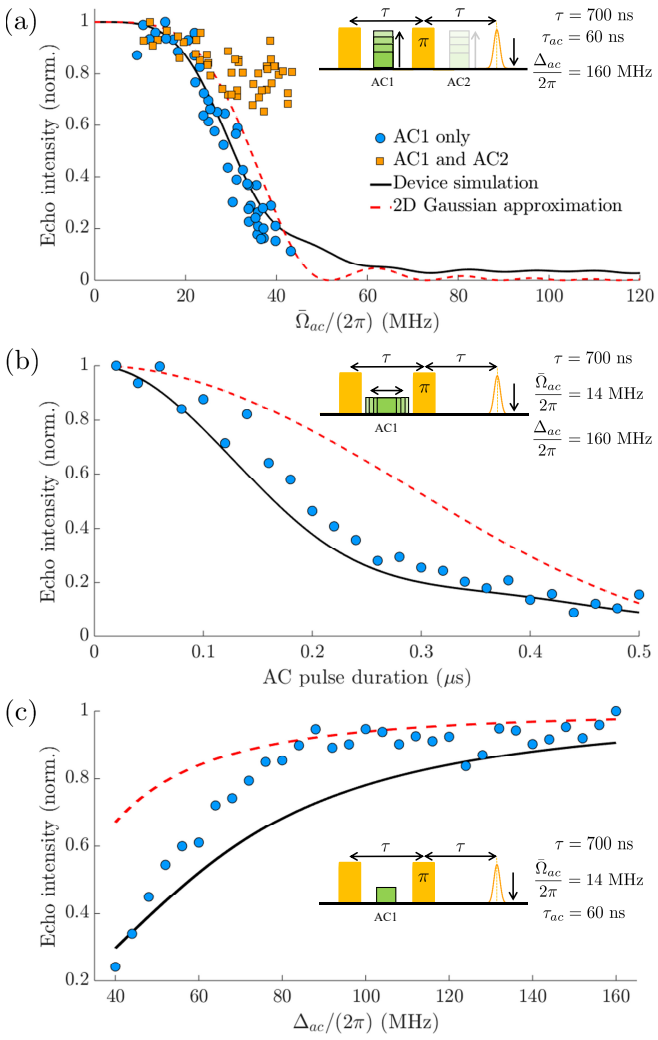

FIG. 3. ACSS control of Nd^{3+} photon echo emission. The echo intensity is plotted against the average ACSS Rabi frequency $\bar{\Omega}_{ac}$ in (a), the ACSS duration τ_{ac} in (b), and the ACSS detuning Δ_{ac} in (c). The insets in each sub-figure illustrate the pulse sequence used. The duration of the input and π pulses in all measurements was 20 ns, and τ represents the pulse-center to pulse-center time separation. The expected echo intensity based on the simulated cavity mode is shown by the solid black curve, and the analytic approximation derived from a 2d Gaussian distribution of the cavity field is shown by the dashed red curve.

coarse approximation that captures the smaller variation of the field envelope along the y-axis in comparison to the variation along the x and z axes (see Figure 1(c)). Despite this, the analytical solution is a useful reference point for understanding the echo behavior. The numerical model used the simulated cavity mode profile from a finite difference time domain calculation (COMSOL), and the ions' frequencies are chosen from a Gaussian distribution with a FWHM equal to the input pulse average Rabi frequency ($\bar{\Omega} = 2\pi \times 25$ MHz) [36]. The model was fitted to the data using one free parameter R: the ratio of the maximum ACSS Rabi frequency $\Omega_{ac}(\boldsymbol{r})_{max}$ to the average ACSS Rabi frequency $\bar{\Omega}_{ac}$. The agreement between the experimental and simulated data for the least squares fit value of $R = 1.83 \pm 0.02$ is further evidence that the ACSS is the dominant perturbation to the system.

With the experimentally determined value for R it is possible to calculate the single photon-ion interaction strength g. From the analysis in Section II A, pulses with an intensity in the cavity of $\langle n \rangle = 0.53$ yielded $\bar{\Omega} = 2\pi \times 25$ MHz. Given that

$$g_{\max} = \frac{\bar{\Omega} R}{2\langle n \rangle^{1/2}} \ , \tag{4}$$

the values of R and $\langle n \rangle$ specified above result in a $g_{\max} = 2\pi \times 31.4$ MHz, which is consistent with previous observations in this device [21]. The value of $g_{\max}$ determined from our experiments also agrees well with the calculated value of

$$\begin{aligned} g_{\text{calc}} &= \frac{\mu}{n}\sqrt{\frac{\omega_0}{2\hbar\varepsilon_0 V}} \\ &= 2\pi \times 27.9 \text{ MHz} \ , \end{aligned} \tag{5}$$

where we have used the transition dipole moment $\mu = 8.48 \times 10^{-32}$ Cm [37], the refractive index $n = 2.1785$ (light polarized parallel to the crystal c axis with wavelength of 879.9 nm) [38], the simulated mode volume of the cavity $V = 0.0564$ μm^3, the transition frequency ω_0, and the vacuum permittivity ε_0. Using the experimentally determined value of $g_{\max}$, the maximum possible single photon ACSS in the cavity at a detuning $\Delta_{ac}/2\pi = 160$ MHz is

$$\begin{aligned} \delta_{ac} &= \frac{2{g_{\max}}^2}{\Delta_{ac}} \\ &= 2\pi \times 12.3 \text{ MHz} \ . \end{aligned} \tag{6}$$

C. Investigation of incomplete echo recovery

To further investigate the incomplete echo recovery seen in Figure 3(a), a variation of the two pulse photon echo sequence was used. In this case, the perturbing ACSS pulse AC1 filled the time between the input and inversion pulses, and AC2 filled the time between the inversion pulse and the echo. The average Rabi frequency used for the ACSS pulses was $\bar{\Omega}_{ac} = 2\pi \times 6.5$ MHz. The results of this measurement are shown in Figure 4 along with insets showing the measurement pulse sequence.

Figure 4(a) shows the data from measurements where the sign of Δ_{ac} was reversed after the inversion pulse. The figure shows that δ_{ac} increases as Δ_{ac} decreases, which results in a more rapid echo decay. In Figure 4(b), AC1 and AC2 both possess the same Δ_{ac}. In an ideal implementation, the phase perturbation due to the ACSS should be balanced and the echo decay should match the

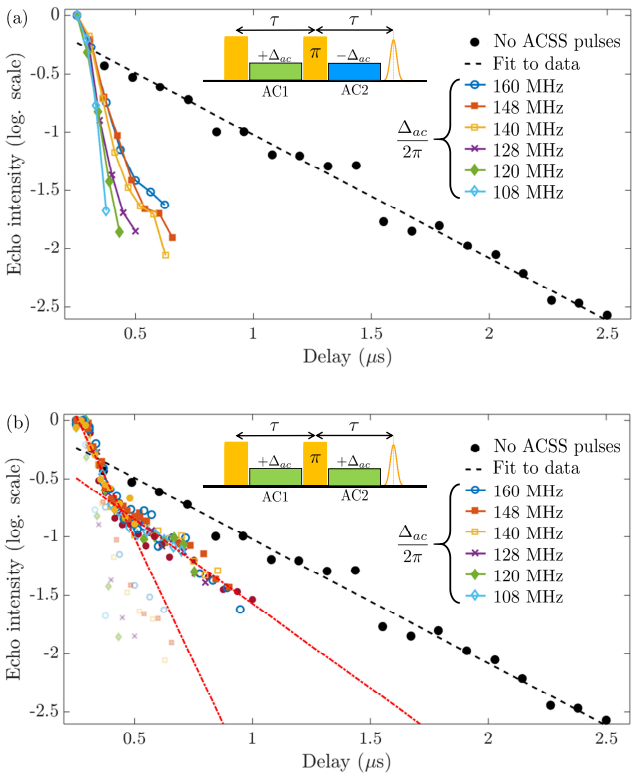

FIG. 4. Two pulse photon echo studies of the ACSS where the pulses AC1 and AC2 are applied between the end of the input (inversion) pulse and the beginning of the inversion pulse (echo). In (a) AC1 and AC2 have detunings Δ_{ac} that have opposite sign, whereas in (b) the detunings are equal. In both cases the black trace (full circles) shows the photon echo decay in the absence of AC1 and AC2 and the other traces represent the data for different values of Δ_{ac}. The red dash-dotted curves are the exponential decay curves of the ACSS measurements for delays $\tau < 400$ ns and $\tau > 400$ ns.

case where no ACSS pulses are applied. In contrast, for delays $\tau < 400$ ns we observed that the echo intensity decayed on a timescale similar to the unbalanced case (the data points from part (a) are superimposed in part (b)). We attribute this rapid decay to the ACSS phase perturbation remaining unbalanced on this time scale. This is likely to be caused by timing jitter due to imperfect alignment of the two AOM double pass setups and intensity fluctuations resulting from the sharp amplitude step functions in the radio frequencies applied to the AOMs.

For delays $\tau > 400$ ns, the decay more closely resembles the unperturbed case. Fitting the echo decay for $\tau > 400$ ns to an exponential decay (shown by the red dash-dotted curve) gives an effective coherence time of 2.8 ± 0.2 μs compared to 3.8 ± 0.2 μs for the unperturbed photon echo measurement. The difference between these decay rates will have contributions due to the residual imbalance between the two ACSS pulses, instantaneous spectral diffusion due to the excitation of residual ion population remaining in the spectral trenches, and device heating.

III. DISCUSSION

A. All-optical hybrid photon echo rephasing memories

The results demonstrate that a single intra-cavity photon can produce an ACSS δ_{ac} that is 100× larger than the Nd^{3+} homogeneous linewidth $\Gamma_h = 84$ kHz. Therefore, maintaining $\langle n \rangle \gg 0.01$ during τ_{ac} allows all-optical control of the relative phases of ions within an ensemble. Thus, this work establishes a path toward realizing all-optical variations of techniques that have previously relied on applied electric fields [27, 28].

In particular, our measurements form the basis for achieving an all-optical quantum memory based on the hybrid photon echo rephasing (HYPER) protocol previously implemented with electric field gradients [30]. The HYPER protocol uses two inversion pulses to recall an input photon (the HYPER echo) when the ensemble is almost completely in the ground state. This avoids the stimulated emission noise that occurs when the recalled photon is emitted while the ensemble is inverted, such as in the case when only a single inversion pulse is used [39]. For HYPER to achieve high efficiency, the intermediate echo resulting from the first inversion is suppressed using an inhomogeneous phase perturbation, which is later rephased to recover the HYPER echo [40]. An ideal implementation of HYPER offers quantum storage using the material's full optical depth and natural bandwidth because no preparation of the inhomogeneous line is necessary.

The photon echo measurements presented in Figure 3 demonstrate two of the important aspects for an all-optical HYPER memory. The first is the suppression of the intermediate echo using the controlled phase perturbation, and the second is the balancing of that phase to allow the formation of the HYPER echo (Figure 3(a)). Both of these aspects are combined in a proof-of-principle demonstration of the HYPER sequence shown in Figure 5, where the secondary echo is enhanced when the balanced ACSS pulses are applied. An all-optical version of HYPER is promising for on-chip quantum memories because additional electrodes on the REI substrate are not required, the efficiency can theoretically approach unity in the limit of an impedance matched cavity (see Appendix B), and Δ_{ac} can be increased so that the storage bandwidth can approach the inhomogeneous linewidth (GHz). A challenge for HYPER memories is to simultaneously achieve high efficiency and high fidelity. To do so requires efficient inversion pulses over the bandwidth of interest, which is not achieved by the simple Gaussian pulses used in this work. Although the use of more complex adiabatic pulses offer a pathway to achieve large bandwidth and efficient inversion [41], the resultant

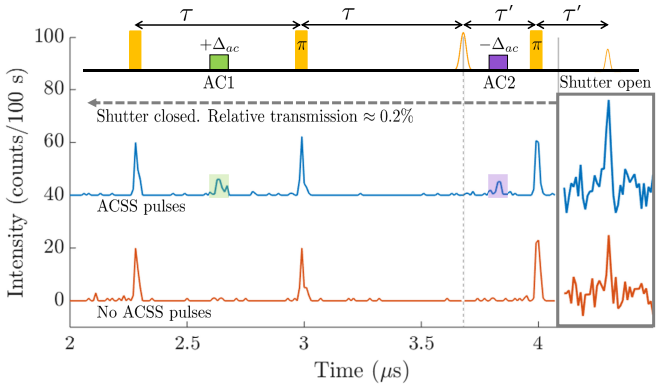

FIG. 5. ACSS controlled HYPER protocol sequence. The lower trace shows the signal when no ACSS pulses are applied, and the upper trace (offset for clarity) shows the signal when both ACSS pulses are applied. Superimposed above the data is the pulse sequence used, where $\tau = 700$ ns, $\tau' = 250$ ns, and $\Delta_{ac} = 160$ MHz. Further details are provided in Appendix A.

instantaneous spectral diffusion may ultimately reduce the maximum storage time of the memory [42].

B. Optically controlled atomic frequency comb memories

Other all-optical quantum protocols are possible in the nanodevices because the δ_{ac} is large compared to the width of absorption features prepared by optical pumping ($\Gamma_f \leq 3$ MHz [21, 31]). As a result it is possible to create an AFC memory with an ACSS controlled readout. Importantly, the ACSS allows control that is not possible using dc electric fields. Although protocols that dynamically alter the comb profile during storage using dc electric fields have been investigated [43], they are not able to achieve a continuously tunable delay. This is because there is no correlation between an ions' spatial position and resonant frequency in stochastically doped crystals. In contrast, the spectral dependence of the ACSS makes it possible to achieve a continuously tunable storage time (see Appendix D). This was demonstrated in Reference 21, where ACSS pulses were applied frequency-symmetrically at large detunings about the AFC center. To realize ACSS controlled AFC memories operating with high efficiency further steps are required. In samples with a uniform distribution of ions the recall efficiency of a pulse stored with a controlled delay will be limited due to the ACSS inhomogeneity [21] (see Supplementary Material). To overcome this limitation requires control of the spatial location of the ions within the cavity either through spectroscopic selection or controlled placement [21].

For both the ACSS controlled HYPER and AFC protocols, operation at the quantum level will require the suppression of noise photons that are generated by ions excited resonantly or off-resonantly by the ACSS control pulses. Therefore, a large single photon ACSS is desirable because the required frequency shift can be achieved with fewer photons, reducing the number of excited ions contributing to the noise. To suppress noise photons that are generated outside the memory bandwidth with high extinction, spectral filters created by optical pumping in another Nd^{3+}:YVO_4 crystal can be applied [2, 44]. For photons generated within the memory bandwidth, a high memory efficiency ensures that these noise photons are time-separated from the signal photon through the protocol storage (see Appendix E).

C. Quantum non-demolition measurements

In addition to offering opportunities for all-optical quantum memories, a large single photon ACSS can be harnessed for quantum non-demolition measurements [29]. Sinclair *et al.* discuss the measurement of the phase shift of an optical probe pulse stored in an AFC due to the ACSS of a single photon transmitted through the cavity in a transparent window adjacent to the memory. The phase shift of the retrieved probe pulse is then a non-destructive measurement that heralds the presence of a single photon. The maximum single photon phase shift resultant from the experiments performed here is 3×10^{-4} rad, which is consistent with the prediction from Reference 29. Ideally, the phase shift would be increased further through longer optical confinement in the cavity. Given the current quality factor of the device ($Q \approx 2.9 \times 10^3$), an order of magnitude improvement should be possible with further optimization of the cavity design and fabrication.

Although an accumulated phase shift can be increased by improving the cavity Q, increasing the single photon interaction strength (the single ion g) requires a significantly lower cavity mode volume or an optical transition with a larger dipole moment. The photon-ion interaction strength achieved in our nanocavities approaches the limit for what can be achieved for REI quantum devices using a conventional photonic crystal structure. This is because the optical dipole moment of Nd^{3+}:YVO_4 is among the largest for 4f $\leftrightarrow$ 4f transitions, and the mode volume of the device studied in this work is within a factor of 10 of the minimum mode volume for conventional dielectric photonic crystal cavities $\approx (\lambda/2n)^3$ [45].

D. Toward larger photon-REI interactions

A relevant next goal is to realize a single photon ACSS that is large compared to the ensemble inhomogeneous linewidth, which is of the order of 100 MHz - 1 GHz. This would allow a single photon to create a phase shift approaching 10^{-2} rad, facilitating single shot, non-destructive quantum measurement, or to tune two ions into resonance with one another. To achieve a single pho-

ton ACSS of this order would require an increase in g by a factor between 3 and 10 (the ACSS is proportional to g^2). One effective strategy to pursue this goal would be to change the cavity design to incorporate dielectric discontinuities [46–48], thereby reducing the mode volume. Previous work in the design of such cavities indicate that a 100× reduction in the mode volume is certainly feasible. A second strategy would be to use the weaker $4f \leftrightarrow 4f$ transition for the storage of photonic qubits and the parity allowed $4f \leftrightarrow 5d$ transitions to perform the ACSS manipulation. The optical dipole moments of the 4f ↔ 5d transitions are of the order of 50× larger than the parity disallowed $4f \leftrightarrow 4f$ transitions, potentially increasing the ac Stark interaction by a factor of over 10^3. Although doubly resonant photonic crystal cavity designs exist [49], integrating two cavities, one of which is required to operate close to the edge of the ultraviolet A band [50], would be challenging. Currently, the most direct path toward such a device would use the hybrid approach that confines the light in a device layer bonded to an active REI substrate [14, 51].

IV. CONCLUSION

In this paper we have demonstrated and characterized a large single photon ACSS of Nd^{3+} ions in a nanophotonic resonator fabricated on a YVO_4 substrate. By combining the relatively large optical dipole moment of the studied transition with the high spatial mode confinement of the on-chip photonic crystal cavity, it is possible to access a new regime for all-optical control in REI crystals. Importantly, the ACSS due to a single photon 160 MHz off-resonance was large compared to both the homogeneous line width and spectral feature width measured in this experiment configuration. Consequently, new opportunities arise for using single photons to control quantum information protocols in this class of materials. Given the results of this work and the avenues for increasing the strength of the interaction, the ACSS is able to extend the versatility of an already appealing physical system for photon-spin integration at the quantum level.

ACKNOWLEDGMENTS

This work was funded by a National Science Foundation (NSF) Faculty Early Career Development Program (CAREER) award (1454607), the AFOSR Quantum Transduction Multidisciplinary University Research Initiative (FA9550-15-1-002), and the Defense Advanced Research Projects Agency Quiness program (W31P4Q-15-1-0012). Equipment funding was also provided by the Institute of Quantum Information and Matter, an NSF Physics Frontiers Center with support from the Moore Foundation. We gratefully acknowledge critical support and infrastructure provided for this work by the Kavli Nanoscience Institute at the California Institute of Technology. J.G.B. acknowledges the support of the American Australian Association's Northrop Grumman Fellowship.

[1] K. R. Ferguson, S. E. Beavan, J. J. Longdell, and M. J. Sellars, Physical Review Letters **117**, 020501 (2016).
[2] K. Kutluer, M. Mazzera, and H. de Riedmatten, Physical Review Letters **118**, 210502 (2017).
[3] C. Laplane, P. Jobez, J. Etesse, N. Gisin, and M. Afzelius, Physical Review Letters **118**, 210501 (2017).
[4] M. P. Hedges, J. J. Longdell, Y. Li, and M. J. Sellars, Nature **465**, 1052 (2010).
[5] M. Gündoğan, P. M. Ledingham, K. Kutluer, M. Mazzera, and H. de Riedmatten, Physical Review Letters **114**, 230501 (2015).
[6] C. Laplane, P. Jobez, J. Etesse, N. Timoney, N. Gisin, and M. Afzelius, New Journal of Physics **18** (2016).
[7] J. J. Longdell and M. J. Sellars, Physical Review A **69**, 032307 (2004).
[8] R. W. Equall, Y. Sun, R. L. Cone, and R. M. Macfarlane, Physical Review Letters **72**, 2179 (1994).
[9] T. Böttger, C. W. Thiel, R. L. Cone, and Y. Sun, Physical Review B **79**, 1 (2009).
[10] M. Zhong, M. P. Hedges, R. L. Ahlefeldt, J. G. Bartholomew, S. E. Beavan, S. M. Wittig, J. J. Longdell, and M. J. Sellars, Nature **517**, 1 (2015).
[11] M. Rančić, M. P. Hedges, R. L. Ahlefeldt, and M. J. Sellars, Nature Physics , 1 (2017).
[12] M. F. Reid, in *Spectroscopic Properties of Rare Earths in Optical Materials*, edited by G. Liu and B. Jacquier (Springer Berlin Heidelberg, 2005).
[13] E. Saglamyurek, N. Sinclair, J. A. Slater, K. Heshami, D. Oblak, and W. Tittel, New Journal of Physics **16**, 065019 (2014).
[14] S. Marzban, J. G. Bartholomew, S. Madden, K. Vu, and M. J. Sellars, Physical Review Letters **115**, 1 (2015).
[15] T. Zhong, J. M. Kindem, E. Miyazono, and A. Faraon, Nature Communications **6**, 8206 (2015).
[16] E. Saglamyurek, M. Grimau Puigibert, Q. Zhou, L. Giner, F. Marsili, V. B. Verma, S. Woo Nam, L. Oesterling, D. Nippa, D. Oblak, and W. Tittel, Nature communications **7**, 11202 (2016).
[17] G. Corrielli, A. Seri, M. Mazzera, R. Osellame, and H. de Riedmatten, Physical Review Applied **5**, 054013 (2016).
[18] T. Zhong, J. Rochman, J. M. Kindem, E. Miyazono, and A. Faraon, Optics Express **24**, 536 (2016).
[19] E. Miyazono, T. Zhong, I. Craiciu, J. M. Kindem, and A. Faraon, Applied Physics Letters **108** (2016), 10.1063/1.4939651.
[20] T. Zhong, J. M. Kindem, J. Rochman, and A. Faraon, Nature Communications **8**, 14107 (2017).

[21] T. Zhong, J. M. Kindem, J. G. Bartholomew, J. Rochman, I. Craiciu, E. Miyazono, M. Bettinelli, E. Cavalli, V. Verma, S. W. Nam, F. Marsili, M. D. Shaw, A. D. Beyer, and A. Faraon, Science **357**, 1392 (2017).

[22] M. Afzelius and C. Simon, Physical Review A **82**, 1 (2010).

[23] S. R. Hastings-Simon, M. U. Staudt, M. Afzelius, P. Baldi, D. Jaccard, W. Tittel, and N. Gisin, Optics Communications **266**, 716 (2006).

[24] N. Sinclair, E. Saglamyurek, M. George, R. Ricken, C. La Mela, W. Sohler, and W. Tittel, Journal of Luminescence **130**, 1586 (2010).

[25] E. Saglamyurek, N. Sinclair, J. Jin, J. A. Slater, D. Oblak, F. Bussières, M. George, R. Ricken, W. Sohler, and W. Tittel, Nature **469**, 512 (2011).

[26] N. Sinclair, D. Oblak, C. W. Thiel, R. L. Cone, and W. Tittel, Physical Review Letters **118**, 100504 (2017).

[27] T. Chanelière and G. Hétet, Optics Letters **40**, 1294 (2015).

[28] H. C. McDonald, *Controlling Photon Echoes with the Light Shift*, Master's thesis, University of Otago (2016), retrieved from http://hdl.handle.net/10523/6787.

[29] N. Sinclair, K. Heshami, C. Deshmukh, D. Oblak, C. Simon, and W. Tittel, Nature Communications **7**, 13454 (2016).

[30] D. L. McAuslan, P. M. Ledingham, W. R. Naylor, S. E. Beavan, M. P. Hedges, M. J. Sellars, and J. J. Longdell, Physical Review A **84**, 1 (2011).

[31] M. Afzelius, M. U. Staudt, H. de Riedmatten, N. Gisin, O. Guillot-Noël, P. Goldner, R. Marino, P. Porcher, E. Cavalli, and M. Bettinelli, Journal of Luminescence **130**, 1566 (2010).

[32] Y. Sun, C. W. Thiel, R. L. Cone, R. W. Equall, and R. L. Hutcheson, Journal of Luminescence **98**, 281 (2002).

[33] S. R. Hastings-Simon, M. Afzelius, J. Minář, M. U. Staudt, B. Lauritzen, H. de Riedmatten, N. Gisin, A. Amari, A. Walther, S. Kröll, E. Cavalli, and M. Bettinelli, Physical Review B **77**, 1 (2008).

[34] D. L. McAuslan, J. J. Longdell, and M. J. Sellars, Physical Review A **80**, 1 (2009).

[35] In the work of Reference 27, balancing ACSS pulses are able to recover the echo intensity with an efficiency of 98%.

[36] The average Rabi frequency ($2\pi \times 25$ MHz) is used because it exceeds the Fourier bandwidth of the 20 ns excitation pulses ($2\pi \times 22.065$ MHz.).

[37] The value of μ is calculated from the published oscillator strength $f = 8 \times 10^{-6}$ [32]. We note that the stated value of the transition dipole moment $\mu = 9.16 \times 10^{-32}$ Cm in Reference 34 appears to have been calculated using the refractive index for light polarized along the a-axis ($n = 1.9682$).

[38] H. S. Shi, G. Zhang, and H. Y. Shen, J. Synth. Cryst **30**, 85 (2001).

[39] J. Ruggiero, J.-L. Le Gouët, C. Simon, and T. Chanelière, Physical Review A **79**, 1 (2009).

[40] V. Damon, M. Bonarota, A. Louchet-Chauvet, T. Chanelière, and J.-L. Le Gouët, New Journal of Physics **13**, 093031 (2011).

[41] L. Rippe, M. Nilsson, S. Kröll, R. Klieber, and D. Suter, Physical Review A **71**, 062328 (2005).

[42] J. Dajczgewand, R. L. Ahlefeldt, T. Böttger, A. Louchet-Chauvet, J.-L. Le Gouët, and T. Chanelière, New Journal of Physics **17**, 23031 (2015).

[43] B. Lauritzen, J. Minář, H. de Riedmatten, M. Afzelius, and N. Gisin, Physical Review A **83**, 1 (2011).

[44] S. E. Beavan, E. A. Goldschmidt, and M. J. Sellars, Journal of the Optical Society of America B **30**, 1173 (2013).

[45] R. Coccioli, M. Boroditsky, K. W. Kim, Y. Rahmat-Samii, and E. Yablonovitch, IEE Proceedings - Optoelectronics **145**, 391 (1998).

[46] J. T. Robinson, C. Manolatou, L. Chen, and M. Lipson, Physical Review Letters **95**, 1 (2005).

[47] S. Hu and S. M. Weiss, ACS Photonics **3**, 1647 (2016).

[48] H. Choi, M. Heuck, and D. Englund, Physical Review Letters **118**, 1 (2017).

[49] K. Rivoire, S. Buckley, and J. Vučković, Optics express **19**, 22198 (2011).

[50] D. Néel, I. Roland, X. Checoury, M. E. Kurdi, S. Sauvage, C. Brimont, T. Guillet, B. Gayral, F. Semond, and P. Boucaud, Advances in Natural Sciences: Nanoscience and Nanotechnology **5**, 023001 (2014).

[51] E. Miyazono, I. Craiciu, A. Arbabi, T. Zhong, and A. Faraon, Opt. Express **25**, 2863 (2017).

Appendix A: Methods

1. Nd^{3+}:YVO_4 nanobeam photonic crystal cavity

The nanophotonic device used in these experiments was the same cavity that was used for the work in Reference 21. For completeness we repeat some of the details of the design and fabrication in this section. The nanobeam is based on a cross section of an equilateral triangle that has a width of 690 nm. First, a suspended triangular prism waveguide is formed through angled focused ion beam milling. Grooves are then milled onto the top surface of the waveguide to form the photonic crystal cavity, each with a width of 147 nm. The groove structure in this device was asymmetric to create a one-sided cavity: 13 grooves on one side of the cavity and 20 grooves on the other. The period of the grooves is increased quadratically for 7 grooves on each side of the cavity mode center to form the mode in the photonic bandgap. The measured quality factor of the resonator was initially $\approx 3.7 \times 10^3$ [21] but had degraded slightly when used for this work ($Q \approx 2.9 \times 10^3$).

2. Optical measurements

The pulse sequences used in this work were created by amplitude modulating the output from a continuous wave Ti:Sapphire laser (M Squared Solstis). The modulation was achieved using a series of two AOMs (Isomet 1250c), both in double pass configuration, and an intensity EOM (Jenoptik). When operating with a pulse duration of 20 ns, the extinction ratio of the total system is approximately 150 dB. The polarization of the light was controlled through a combination of fiber and free space polarization optics, which ensured the light entering the waveguide was polarization matched to the TM mode. The substrate with the nanodevice was mounted onto a 3-axis nanopositioning stage (Attocube), which was loaded into a ^{3}He dilution refrigerator (BlueFors). Light was coupled into and out of the waveguide by focusing onto a 45° surface at the end of the waveguide. The APD (Perkin Elmer) was protected from the bright excitation and rephasing pulses using a third AOM as a shutter. The shutter provided an attenuation of ≈23 dB.

Before each of the photon echo and HYPER measurements, transparent features were prepared at the ACSS frequency through optical pumping. The optical pumping was performed by exciting the ions at $\omega_p + \Delta_{ac}$ with >1000 π pulses separated by 20 μs. The laser was then gated off for a further 250 μs ($> 50\times$ the excited state lifetime in the cavity) to ensure that there was no population remaining in the excited state. The measurement sequence was then repeated 400 times at a repetition rate of ≈100 kHz. The combined optical pumping and measurement sequence was repeated at a rate of 20 Hz. Signals were integrated over 100 s.

For the data presented in Figure 5, the photon counts are binned in 10 ns time bins. For the region showing the HYPER echo, the background due to incoherent emission has been subtracted from the data for clarity.

For the Rabi flopping data presented in Figure 2, 8×10^3 two pulse echo sequences were performed per second in bursts of 400 separated by a wait time of 40 ms. This was repeated over a duration of 20 s and the echo intensity detected on the APD. The input pulse duration was constant (20 ns) and the time separation between the centers of the input and second pulse was maintained at 500 ns.

Appendix B: Cavity Maxwell-Bloch equations for generalized all-optical HYPER sequence

The all-optical HYPER sequence is divided into 9 sections as shown in Figure 6. It is assumed that the laser pulse sequence is incident on a perfectly one-sided optical cavity that contains an ensemble of N rare-earth ions. Let the cavity decay rate (field) be κ and the single photon Rabi frequency to be g. Each ion has a homogeneous linewidth 2γ and a detuning Δ from the input pulse frequency (shown in orange in Figure 6). The ion ensemble has an inhomogeneous distribution $\rho(\Delta)$ with a FWHM γ_{ih} such that $\int \rho(\Delta) d\Delta = N$, with N the total number of ions. Initially it is assumed that the cavity field is equal at the spatial location of each ion. We will later relax this assumption, which will give rise to the ability to control the coherent emission from the cavity-coupled ensemble. The uniform ac Stark shift (ACSS) resulting from ACSS pulses AC1, AC2, and AC3, is denoted δ_1, δ_2, and δ_3, respectively.

The equations of motion for the coupled ion-cavity system in each of the regions I-IX are written below, where the $\varepsilon_i(t)$ and $\sigma_i(t)$ are the cavity field and the atomic polarizations (for a given Δ), respectively.

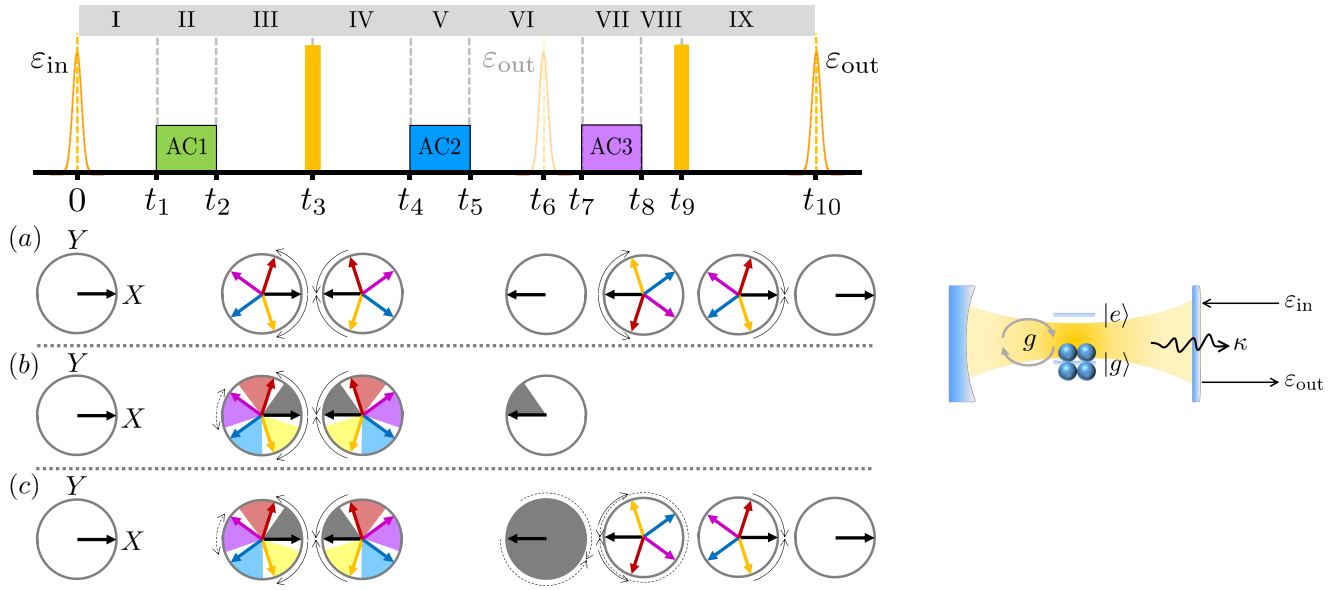

FIG. 6. (left) Generalized pulse sequence for an all-optical variant of the HYPER quantum memory protocol. The pulses at t_3 and t_9 are assumed to be perfect inversion pulses. The ensemble emission ε_{out} in Region VI is the two pulse photon echo that the HYPER sequence seeks to suppress. The three panels (a), (b), and (c) give a perspective of how the optical Bloch vectors evolve in the equatorial plane of the Bloch sphere for the HYPER pulse sequence under different ACSS conditions. In (a), no ACSS pulses are applied. The different colored vectors represent ensemble sub-groups that accumulate phase according to their detuning (shown by the solid black arrows). Part (b) shows the sequence applied in the main article for characterizing the ACSS where only AC1 is applied. The result is an inhomogeneous phase evolution determined by the ACSS (colored segments and dashed arrows). Although the inversion pulse rephases the fixed inhomogeneity, the ACSS-induced inhomogeneity remains and the echo intensity is reduced (the Bloch vectors do not fully rephase). In part (c), all three ACSS pulses are applied, with the combined effect of AC1 and AC2 suppressing the intermediate echo in Region VI, but balanced by the effect of AC3 to recover complete rephasing in Region IX. (right) Schematic of the one-sided cavity assumed in the derivation.

$$
\begin{aligned}
&I: \\
&\quad \dot{\varepsilon}_I = -\kappa\varepsilon_I + \sqrt{2\kappa}\varepsilon_{\text{in}} + ig\int \rho(\Delta)\sigma_I d\Delta \ , \\
&\quad \dot{\sigma}_I = -i\Delta\sigma_I - \gamma\sigma_I + ig\varepsilon_I \ , \\
&\quad \sigma_I(0) = 0 \ , \\
&II: \\
&\quad \dot{\sigma}_{II} = -i(\Delta+\delta_1)\sigma_{II} - \gamma\sigma_{II} \ , \\
&\quad \sigma_{II}(t_1) = \sigma_I(t_1) \ , \\
&III: \\
&\quad \dot{\sigma}_{III} = -i\Delta\sigma_{III} - \gamma\sigma_{III} \ , \\
&\quad \sigma_{III}(t_2) = \sigma_{II}(t_2) \ , \\
&IV: \\
&\quad \dot{\sigma}_{IV} = -i\Delta\sigma_{IV} - \gamma\sigma_{IV} \ , \\
&\quad \sigma_{IV}(t_3) = \sigma^*_{III}(t_3) \ , \\
&V: \\
&\quad \dot{\sigma}_V = -i(\Delta+\delta_2)\sigma_V - \gamma\sigma_V \ , \\
&\quad \sigma_V(t_4) = \sigma_{IV}(t_4) \ ,
\end{aligned}
$$

$$
\begin{aligned}
&VI: \\
&\quad \dot{\varepsilon}_{VI} = -\kappa\varepsilon_{VI} + ig\int \rho(\Delta)\sigma_{VI}d\Delta \ , \\
&\quad \dot{\sigma}_{VI} = -i\Delta\sigma_{VI} - \gamma\sigma_{VI} - ig\varepsilon_{VI} \ , \\
&\quad \sigma_{VI}(t_5) = \sigma_V(t_5) \ , \\
&VII: \\
&\quad \dot{\sigma}_{VII} = -i(\Delta+\delta_3)\sigma_{VII} - \gamma\sigma_{VII} \ , \\
&\quad \sigma_{VII}(t_7) = \sigma_{VI}(t_7) \ , \\
&VIII: \\
&\quad \dot{\sigma}_{VIII} = -i\Delta\sigma_{VIII} - \gamma\sigma_{VIII} \ , \\
&\quad \sigma_{VIII}(t_8) = \sigma_{VII}(t_8) \ , \\
&IX: \\
&\quad \dot{\varepsilon}_{IX} = -\kappa\varepsilon_{IX} + ig\int \rho(\Delta)\sigma_{IX}d\Delta \ , \\
&\quad \dot{\sigma}_{IX} = -i\Delta\sigma_{IX} - \gamma\sigma_{IX} + ig\varepsilon_{IX} \ , \\
&\quad \sigma_{IX}(t_9) = \sigma^*_{VIII}(t_9) \ .
\end{aligned}
$$

Region I

The general solution for the atomic polarization is

$$\sigma_I(t) = e^{(-\gamma-i\Delta)t}K + ige^{(-\gamma-i\Delta)t}\int_{-\infty}^{t} e^{(\gamma+i\Delta)t'}\varepsilon_I(t')dt' \ . \tag{B1}$$

The boundary condition gives $K = 0$. Therefore,

$$\sigma_I(t) = ige^{(-\gamma-i\Delta)t}\int_{-\infty}^{t} e^{(\gamma+i\Delta)t'}\varepsilon_I(t')dt' \ . \tag{B2}$$

Substituting the solution into the equation of motion for the cavity field gives

$$
\begin{aligned}
\dot{\varepsilon}_I &= -\kappa\varepsilon_I + \sqrt{2\kappa}\varepsilon_{\rm in} + ig\int_{-\infty}^{\infty}\rho(\Delta)ige^{(-\gamma-i\Delta)t}\int_{-\infty}^{t} e^{(\gamma+i\Delta)t'}\varepsilon_I(t')dt'd\Delta \ , \\
&= -\kappa\varepsilon_I + \sqrt{2\kappa}\varepsilon_{\rm in} - g^2\int_{-\infty}^{t} e^{-\gamma(t-t')}\varepsilon_I(t')\int_{-\infty}^{\infty}\rho(\Delta)e^{-i\Delta(t-t')}d\Delta dt' \ , \\
&= -\kappa\varepsilon_I + \sqrt{2\kappa}\varepsilon_{\rm in} - g^2\int_{-\infty}^{t} e^{-\gamma(t-t')}\varepsilon_I(t')\tilde{\rho}(t-t')dt' \ , \\
&\approx -\kappa\varepsilon_I + \sqrt{2\kappa}\varepsilon_{\rm in} - C\kappa\varepsilon_I \ ,
\end{aligned} \tag{B3}
$$

where we make the approximation that $\gamma_{\rm ih}$ is much larger than γ and the bandwidth of the input field. Under this approximation the decoherence term $e^{-\gamma(t-t')}$ is negligible on timescales less than $1/\gamma$, and $\tilde{\rho}(t-t') \approx N\delta(t-t')/\gamma_{\rm ih}$. We also introduce the cooperativity $C = g^2N/\kappa\gamma_{\rm ih}$.

Using the fact that

$$\varepsilon_{\rm out} = -\varepsilon_{\rm in} + \sqrt{2\kappa}\varepsilon_I \ , \tag{B4}$$

the steady state solutions of Equation B3 are then

$$
\begin{aligned}
\varepsilon_I &= \frac{\sqrt{2\kappa}}{\kappa(1+C)}\varepsilon_{\rm in} \ , \text{and} \\
\varepsilon_{\rm out} &= \frac{(1-C)}{(1+C)}\varepsilon_{\rm in} \ .
\end{aligned} \tag{B5}
$$

Region II

Similarly to the treatment of Region I, the general solution for the atomic polarization is

$$\sigma_{II}(t) = e^{(-\gamma - i(\Delta+\delta_1))t}K \ , \tag{B6}$$

with the boundary condition defining the value of K. The solution is then written

$$\sigma_{II}(t) = ige^{(-\gamma-i\Delta)t}e^{-i\delta_1(t-t_1)}\int_{-\infty}^{t_1} e^{(\gamma+i\Delta)t'}\varepsilon_I(t')dt' \ . \tag{B7}$$

Region III

Again we have the general solution

$$\sigma_{III}(t) = e^{(-\gamma-i\Delta)t}K \ . \tag{B8}$$

with the boundary condition fixing the solution as

$$\begin{aligned}\sigma_{III}(t) &= ige^{(-\gamma-i\Delta)t}e^{-i\delta_1(t_2-t_1)}\int_{-\infty}^{t_1} e^{(\gamma+i\Delta)t'}\varepsilon_I(t')dt' \ , \\ &= ige^{(-\gamma-i\Delta)t}e^{-i\delta_1\tau_1}\int_{-\infty}^{t_1} e^{(\gamma+i\Delta)t'}\varepsilon_I(t')dt' \ ,\end{aligned} \tag{B9}$$

where τ_1 is defined as $(t_2 - t_1)$, the length of pulse AC1.

Region IV

Using the same procedure, the solutions to Regions IV and V can be written down directly.

$$\sigma_{IV}(t) = -ige^{(-\gamma-i\Delta)t}e^{i\delta_1\tau_1}\int_{-\infty}^{t_1} e^{(\gamma-i\Delta)t'+2i\Delta t_3}\varepsilon_I^*(t')dt' \ . \tag{B10}$$

Region V

$$\sigma_V(t) = -ige^{(-\gamma-i\Delta)t}e^{i\delta_1\tau_1}e^{-i\delta_2(t-t_4)}\int_{-\infty}^{t_1} e^{(\gamma-i\Delta)t'+2i\Delta t_3}\varepsilon_I^*(t')dt' \ . \tag{B11}$$

Region VI

In Region VI, there is the possibility for the ensemble rephasing to generate emission. Therefore, the general solution for the atomic polarization is

$$\sigma_{VI}(t) = e^{(-\gamma-i\Delta)t}K - ige^{(-\gamma-i\Delta)t}\int_{-\infty}^{t} e^{(\gamma+i\Delta)t'}\varepsilon_{VI}(t')dt' \ . \tag{B12}$$

In this region, the boundary condition gives,

$$\sigma_{VI}(t) = -ige^{(-\gamma - i\Delta)t} e^{i\delta_1\tau_1} e^{-i\delta_2\tau_2} \int_{-\infty}^{t_1} e^{(\gamma - i\Delta)t' + 2i\Delta t_3} \varepsilon_I^*(t')dt' \\ -ige^{(-\gamma - i\Delta)t} \int_{t_5}^{t} e^{(\gamma + i\Delta)t'} \varepsilon_{VI}(t')dt' \ , \tag{B13}$$

where τ_2 is defined as $(t_5 - t_4)$, the length of pulse AC2.

Substituting the solution into the equation of motion for the cavity field gives

$$\begin{aligned} \dot{\varepsilon}_{VI} &= -\kappa\varepsilon_{VI} + ig \Big(-ig \int_{-\infty}^{t_1} e^{-\gamma(t-t')} e^{i\delta_1\tau_1} e^{-i\delta_2\tau_2} \varepsilon_I^*(t') \int_{-\infty}^{\infty} \rho(\Delta) e^{-i\Delta(t+t'-2t_3)} d\Delta dt' \\ &\qquad -ig \int_{t_5}^{t} e^{-\gamma(t-t')} \varepsilon_{VI}(t') \int_{-\infty}^{\infty} \rho(\Delta) e^{-i\Delta(t-t')} d\Delta dt' \Big) \ , \\ &= -\kappa\varepsilon_{VI} + g^2 \Big(\int_{-\infty}^{t_1} e^{-\gamma(t-t')} e^{i\delta_1\tau_1} e^{-i\delta_2\tau_2} \varepsilon_I^*(t') \tilde{\rho}(t + t' - 2t_3) dt' \\ &\qquad \int_{t_5}^{t} e^{-\gamma(t-t')} \varepsilon_{VI}(t') \tilde{\rho}(t - t') dt' \Big) \ , \\ &\approx -\kappa\varepsilon_{VI} + 2C\kappa e^{i\delta_1\tau_1} e^{-i\delta_2\tau_2} \varepsilon_I^*(2t_3 - t) + C\kappa\varepsilon_{VI}(t) \ . \end{aligned} \tag{B14}$$

The steady state solutions of Equation B14 are:

$$\begin{aligned} \varepsilon_{VI}(t) &= \frac{2C}{1-C} e^{i\delta_1\tau_1} e^{-i\delta_2\tau_2} e^{-\gamma t} \varepsilon_I^*(2t_3 - t) \ , \text{and} \\ \varepsilon_{\text{out}}(t) &= \frac{4C}{(1-C^2)} e^{i\delta_1\tau_1} e^{-i\delta_2\tau_2} e^{-\gamma t} \varepsilon_{\text{in}}^*(2t_3 - t) \ . \end{aligned} \tag{B15}$$

Region VII

The same procedure as detailed in the preceding Regions are used to write down the solutions for Regions VII, $VIII$, and IX.

$$\begin{aligned}\sigma_{VII}(t) = &-ige^{(-\gamma-i\Delta)t}e^{-i\delta_3(t-t_7)}e^{i\delta_1\tau_1}e^{-i\delta_2\tau_2}\int_{-\infty}^{t_1} e^{(\gamma-i\Delta)t'+2i\Delta t_3}\varepsilon_I^*(t')dt' \\ &-ige^{(-\gamma-i\Delta)t}e^{-i\delta_3(t-t_7)}\int_{t_5}^{t_7} e^{(\gamma+i\Delta)t'}\varepsilon_{VI}(t')dt'\end{aligned} \tag{B16}$$

Region $VIII$

$$\begin{aligned}\sigma_{VIII}(t) = &-ige^{(-\gamma-i\Delta)t}e^{-i\delta_3\tau_3}e^{i\delta_1\tau_1}e^{-i\delta_2\tau_2}\int_{-\infty}^{t_1} e^{(\gamma-i\Delta)t'+2i\Delta t_3}\varepsilon_I^*(t')dt' \\ &-ige^{(-\gamma-i\Delta)t}e^{-i\delta_3\tau_3}\int_{t_5}^{t_7} e^{(\gamma+i\Delta)t'}\varepsilon_{VI}(t')dt' \ ,\end{aligned} \tag{B17}$$

where τ_3 is defined as $(t_8 - t_7)$, the length of pulse AC3.

Region IX

$$\begin{aligned}\sigma_{IX}(t) = &\ ige^{-i\delta_1\tau_1}e^{i\delta_2\tau_2}e^{-i\delta_3\tau_3}\int_{-\infty}^{t_1} e^{-\gamma(t-t')}e^{-i\Delta(t+2t_3-2t_9-t')}\varepsilon_I(t')dt' \\ &+ ige^{-i\delta_3\tau_3}\int_{t_5}^{t_7} e^{-\gamma(t-t')}e^{-i\Delta(t'+t-2t_9)}\varepsilon_{VI}^*(t')dt' \\ &+ ig\int_{t_9}^{t} e^{-\gamma(t-t')}e^{-i\Delta(t-t')}\varepsilon_{IX}(t')dt'\end{aligned} \tag{B18}$$

Substituting the solution into the equation of motion for the cavity field gives

$$\dot{\varepsilon}_{IX}(t) = -\kappa\varepsilon_{IX}(t) - 2C\kappa e^{-\gamma t}e^{-i(\delta_1\tau_1-\delta_2\tau_2+\delta_3\tau_3)}\varepsilon_I(t+2t_3-2t_9) - 2C\kappa e^{-\gamma t}e^{-i\delta_3\tau_3}\varepsilon_{VI}^*(t-2t_9) - C\kappa\varepsilon_{IX}(t) \ . \tag{B19}$$

Under the assumption that all ions are driven by the same field (there is no inhomogeneity in δ_1, δ_2, or δ_3), the term $e^{-i(\delta_1\tau_1-\delta_2\tau_2+\delta_3\tau_3)}$ is simply a phase shift of the emitted HYPER echo. In the next section we will discuss how the inhomogeneity of the cavity field impacts this behavior.

It is also worthwhile to write down the specific solution that represents an efficient HYPER protocol. That is, when $\delta_1\tau_1 - \delta_2\tau_2 + \delta_3\tau_3 = 0$ and ε_{VI} is suppressed, the steady state solutions of Equation B19 around $t = 2(t_9 - t_3)$ are:

$$\begin{aligned}\varepsilon_{IX}(t) &= -\frac{2C}{1+C}e^{-\gamma t}\varepsilon_I(0) \ \text{, and} \\ \varepsilon_{\text{out}}(t) &= -\frac{4C}{(1+C)^2}e^{-\gamma t}\varepsilon_{\text{in}}(0) \ .\end{aligned} \tag{B20}$$

Spatial inhomogeneity

In this section we consider the impact of the field inhomogeneity within the optical cavity. This inhomogeneity can be used to suppress ε_{VI} to achieve an efficient HYPER echo. The photon-ion interaction is represented by the coupling parameter $g(\boldsymbol{r})$:

$$\begin{aligned} g(\boldsymbol{r}) &= \frac{\mu}{n}\sqrt{\frac{\omega}{2\hbar\epsilon_0 V}}\frac{E(\boldsymbol{r})}{\max(E(\boldsymbol{r}))} \\ &= g_0\psi(\boldsymbol{r}) \ , \end{aligned} \tag{B21}$$

where μ is the optical transition dipole moment, n is the refractive index of the material, ω is the transition frequency of the ion (assumed to be in resonance with the cavity), ϵ_0 is the vacuum permittivity, V is the mode volume of the cavity, and $\psi(\boldsymbol{r})$ is the function describing the field amplitude as a function of position. Equation B21 also assumes that the dipole moment is aligned with the electric field $\boldsymbol{E}$ in the cavity. The Rabi frequency can then be expressed as

$$\Omega(\boldsymbol{r}) = 2\sqrt{\langle n_p\rangle}g(\boldsymbol{r}) \ , \tag{B22}$$

where $\langle n_p\rangle$ is the average number of photons in the cavity.

The equations of motion for Region I must be rewritten to incorporate the spatial inhomogeneity of the electric field

$$\begin{aligned} &I: \\ &\dot{\varepsilon}_I = -\kappa\varepsilon_I + \sqrt{2\kappa}\varepsilon_{\text{in}} + \frac{i}{V}\int_V \left(g(\boldsymbol{r})\int \rho(\Delta)\sigma_I d\Delta\right)d\boldsymbol{r} \ , \\ &\dot{\sigma}_I = -i\Delta\sigma_I - \gamma\sigma_I + ig(\boldsymbol{r})\varepsilon_I \ , \\ &\sigma_I(0) = 0 \ . \end{aligned}$$

Here the $\int_V$ represents integration over the cavity mode of volume V.

The solution in Region I has the same form as Equation B5

$$\varepsilon_{\text{out}} = \frac{(1-C)}{(1+C)}\varepsilon^*_{\text{in}} \ . \tag{B23}$$

When $\Delta_{ac} \gg \gamma_{ih}$, δ_1 and δ_2 only depend on an ions position $\boldsymbol{r}$ and not on their frequency Δ. The modified solution for the case of spatial inhomogeneity in Region VI is

$$\varepsilon_{\text{out}}(t) = \frac{4C}{(1-C^2)}\frac{1}{V}\int_V \psi^2(\boldsymbol{r})e^{i\delta_1(\boldsymbol{r})\tau_1}e^{-i\delta_2(\boldsymbol{r})\tau_2}d\boldsymbol{r}e^{-\gamma t}\varepsilon^*_{\text{in}}(2t_3 - t) \ . \tag{B24}$$

Therefore, the amplitude of the first output echo is proportional to

$$\eta = \int_V \psi^2(\boldsymbol{r})e^{i\delta_1(\boldsymbol{r})\tau_1}e^{-i\delta_2(\boldsymbol{r})\tau_2}d\boldsymbol{r} \ . \tag{B25}$$

Because there is no analytical expression for the cavity mode profile $\psi(\boldsymbol{r})$ for the nanocavity used in this work, we calculate the dependence of the echo intensity numerically from the simulated mode profile. In addition, below we use an approximation of $\psi(\boldsymbol{r})$ to form an analytically tractable solution.

The mode envelope of the photonic nanocavity can be approximated by a two-dimensional Gaussian

$$\psi(\boldsymbol{x},\boldsymbol{y},\boldsymbol{z}) \approx e^{-\frac{x^2}{2{\Delta_x}^2}-\frac{z^2}{2{\Delta_z}^2}} \ . \tag{B26}$$

Transforming to polar coordinates allows $\psi(\boldsymbol{x},\boldsymbol{y},\boldsymbol{z})$ to be written as

$$\psi(\boldsymbol{r}) \approx e^{-r^2} \ . \tag{B27}$$

In the case where only AC1 is applied and $\Delta_{ac} \gg \Omega$, Equation B25 becomes

$$\eta \approx \int_0^\infty r e^{-2r^2} e^{-iAe^{-2r^2}} dr \ , \tag{B28}$$

where

$$A = \frac{2\langle n \rangle {g_0}^2 \tau_1}{\Delta_{ac}} \ , \tag{B29}$$

which is the maximum value of the ACSS induced phase shift in the cavity $\max(\phi_{ac})$.

Therefore, the output echo field will be proportional to

$$\eta \propto \frac{e^{-i\max(\phi_{ac})} - 1}{i\max(\phi_{ac})} \ , \tag{B30}$$

and the output echo intensity will be proportional to

$$|\eta|^2 \propto \mathrm{sinc}^2 \left[\frac{\max(\phi_{ac})}{2} \right] \ . \tag{B31}$$

Appendix C: Effect of ensemble averaging in ACSS measurements

For the data shown in Figure 3, each photon echo sequence was accumulated for 100 s and the repetition rate of the measurement sequence was 20 Hz. Thus, the signal represents an average of $8{\times}10^5$ individual photon echoes. Each photon echo sequence will probe a different ensemble of ions within the device. This is due to the combination of the slow laser drift of the order of 10 MHz/hour, the probabilistic excitation of ions within the the input pulse bandwidth, the imperfect inversion of the applied π pulses, and the optical pumping resulting from optical relaxation to the other Zeeman ground state. As a result, the experimental data shown in Figure 3 (and repeated here in Figure 7) represents the average of many ensembles, all of which have different frequency and spatial distributions.

Also included here in Figure 7 is the predicted signal for the pulse sequences used in this work if only a single ensemble was probed. The most important impact of using a single ensemble is that the echo intensity can be attenuated to zero, which is important for applications such as the HYPER memory protocol. In the case where the signal is the result of averaging over many ensembles, the echo intensity only approaches zero in the limit of very large ACSS induced phase shifts.

Experimentally, there are several ways in which to move toward using only a single ensemble. First, eliminating long term laser drift by locking the laser to a stable reference can remove the frequency variation. Second, increasing the photon echo efficiency by engineering complete absorption of the input pulse and by achieving better inversion efficiency reduces the probabilistic processes in the echo signal. Third, a combination of reducing the device temperature, reducing the linewidth of the cavity, and reducing the repetition rate can assist in mediating the ensemble variation due to optical pumping. It is unlikely that all ensemble variation can be removed completely however, the changes in the probed ensemble can be minimized allowing for effective attenuation of the echo intensity using the ACSS.

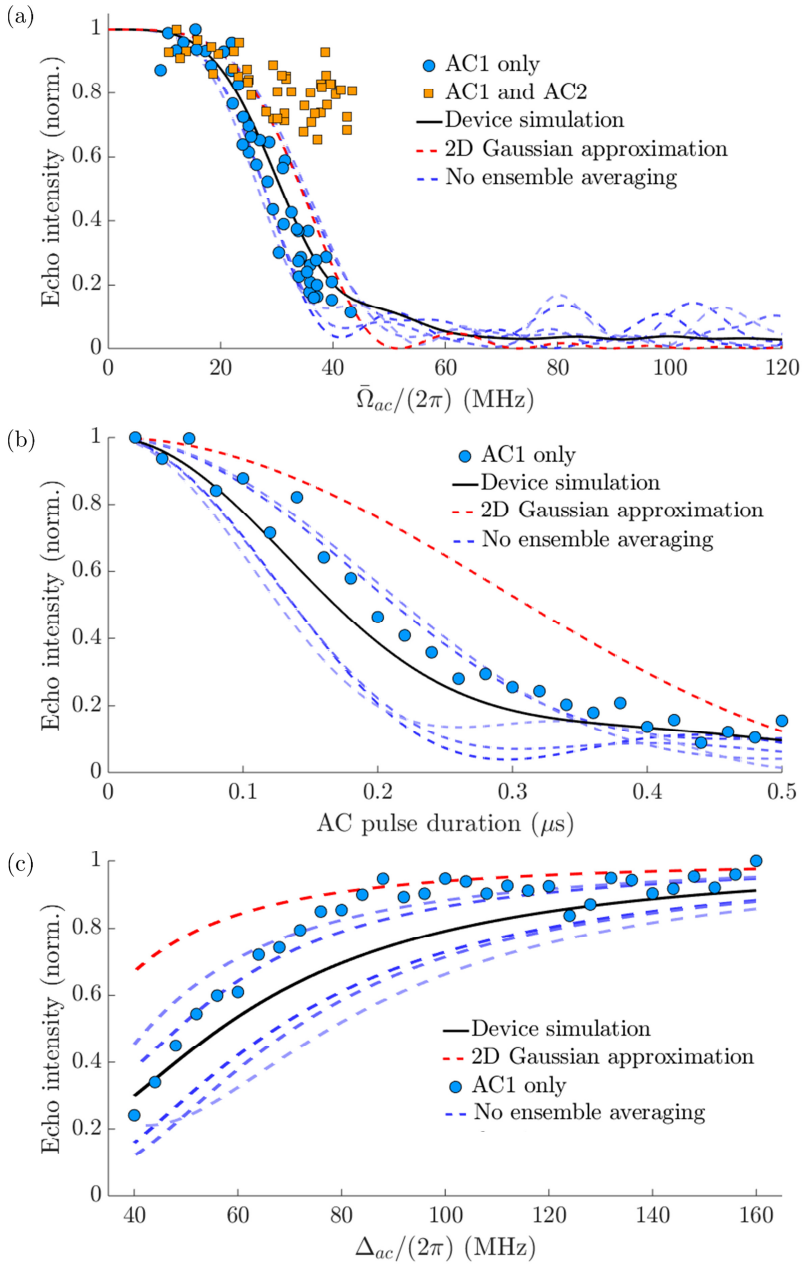

FIG. 7. The effect of ensemble averaging on the experimental data in the main article. Parts (a), (b), and (c) show the data from the main article with the addition of traces that illustrate the expected echo intensity when probing a single ensemble. Each blue dashed trace shows the expected signal from a fixed ensemble in which the frequency and spatial distributions of the ions sample the inhomogeneously broadened line of the Nd^{3+}:YVO_4 sample and the device used in the experiments, respectively.

Appendix D: ACSS-controlled AFC Memory

Here we provide a brief outline of the cavity Maxwell-Bloch equations for the ACSS-controlled AFC quantum memory, based on the work in References 22 and 21. Equation 1 from Reference 22 describes the general time evolution of the cavity field $\varepsilon(t)$

$$\dot{\varepsilon}(t) = -\kappa\varepsilon(t) - \sqrt{2\kappa}\varepsilon_{\text{in}} + i\tilde{\mu}\int d\Delta\rho(\Delta)\sigma_{\Delta}(t) \ , \tag{D1}$$

where κ is the cavity field decay rate, ε_{in} is the input field, $\rho(\Delta)$ is the inhomogeneous atomic spectral distribution (the frequency comb), and $\sigma_{\Delta}(t)$ is the time dependent atomic polarization at detuning Δ. The constant $\tilde{\mu} = \mu\omega_0/2\epsilon_0 V$, where μ is the dipole moment of the optical transition, ω_0 is the cavity frequency, and V is the cavity mode volume. By inserting the solution for the time varying atomic polarization σ_{Δ}, Afzelius et al. [22] write in Equation 8

$$\dot{\varepsilon}(t) = -\kappa\varepsilon(t) + \frac{\mu\tilde{\mu}}{\sqrt{2\kappa}}\int_{-\infty}^{0} dt'\tilde{\rho}(t-t')\varepsilon_{\text{in}}(t') - \mu\tilde{\mu}\int_{0}^{t} dt'\tilde{\rho}(t-t')\varepsilon(t') \ , \tag{D2}$$

where $\tilde{\rho}(t)$ is the Fourier transform of $\rho(\Delta)$.

Here we rewrite Equation D2 using the single photon Rabi frequency g rather than μ and $\tilde{\mu}$ such that

$$\dot{\varepsilon}(t) = -\kappa\varepsilon(t) + \frac{g^2}{\sqrt{2\kappa}}\int_{-\infty}^{0} dt'\tilde{\rho}(t-t')\varepsilon_{\text{in}}(t') - g^2\int_{0}^{t} dt'\tilde{\rho}(t-t')\varepsilon(t') \ . \tag{D3}$$

Around the time at which the AFC echo is formed ($t = 2\pi/\Delta_{\text{afc}}$) in the case where no ACSS pulses are applied, Equation D3 leads to the solution as given in Equation 10 of Reference 22 under the impedance matching condition:

$$\varepsilon_{\text{out}}(t) = -\sqrt{\eta_f}\varepsilon_{\text{in}}(t - \frac{2\pi}{\Delta_{\text{afc}}}) \ , \tag{D4}$$

where η_f is the reduction of the echo efficiency due to the finite width of the comb teeth. The impedance matched condition means $\kappa = \Gamma$, where Γ is the absorption rate of the cavity field by the atomic ensemble. For completeness, $\Gamma = N\mu\tilde{\mu}/\gamma_{\text{ih}} = Ng^2/\gamma_{\text{ih}}$, where N is the total number of ions, and γ_{ih} is the inhomogeneous linewidth of $\rho(\Delta)$. Note that $\kappa = \Gamma$ is equivalent to a unit collective cooperativity $C = Ng^2/\kappa\gamma_{\text{ih}} = 1$.

The effect of the ACSS pulses is to impart an accumulated phase on σ_{Δ} during the phase evolution of all excited dipoles. This phase term is written as $\exp[-i\delta(\Delta,\boldsymbol{r})\tau]$, where $\delta(\Delta,\boldsymbol{r})$ is the ACSS that depends on the ions frequency and spatial position, and τ is the duration of the ACSS pulse. The frequency and spatial degrees of freedom are independent, that is, the frequency of an ion is not dependent on its location within the cavity. When the ACSS pulses are applied symmetrically in frequency about the center of the AFC, and $\Delta_{ac} \gg \Delta_{afc}$, we have

$$\begin{aligned}\delta(\Delta,\boldsymbol{r}) &= -\frac{4\langle n\rangle g(\boldsymbol{r})^2\Delta}{{\Delta_{ac}}^2 - \Delta^2} \\ &\approx -\frac{4\langle n\rangle {g_0}^2\psi(\boldsymbol{r})^2\Delta}{{\Delta_{ac}}^2} \\ &\equiv B\ \psi(\boldsymbol{r})^2\Delta \ ,\end{aligned} \tag{D5}$$

where $B = -4\langle n\rangle {g_0}^2/\Delta_{ac}^2$.

Since the ACSS phase is linear with frequency, when incorporated into the Fourier transform used to derive Equation D3, it causes a time shift of the echo field that is dependent on the location of the ions that emit it. The solution is

$$\dot{\varepsilon}(t) = -\kappa\varepsilon(t) + \frac{{g_0}^2}{V}\int_V \left[\frac{\psi(\boldsymbol{r})^2}{\sqrt{2\kappa}}\int_{-\infty}^{0} dt'\tilde{n}(t-t'+B\ \psi(\boldsymbol{r})^2)\varepsilon_{\text{in}}(t') - \psi(\boldsymbol{r})^2\int_{0}^{t} dt'\tilde{n}(t-t')\varepsilon(t')\right] d\boldsymbol{r} \ . \tag{D6}$$

The output signal is given by

$$\varepsilon_{\text{out}}(t) = -\frac{\sqrt{\eta_f}}{V}\int_V \psi(\boldsymbol{r})^2\varepsilon_{\text{in}}(t - \frac{2\pi}{\Delta_{afc}} + B\ \psi(\boldsymbol{r})^2)d\boldsymbol{r} \ , \tag{D7}$$

where we have assumed impedance matching $C = 1$. In the limit of vanishing inhomogeneity ($\psi(\boldsymbol{r}) \approx 1$) and perfect impedance matching, the input pulse is recalled at a time $t = 2\pi/\Delta_{afc} - B$, a delay of $4\langle n\rangle {g_0}^2/\Delta_{ac}^2$ compared to the unperturbed comb. When $\psi(\boldsymbol{r})$ is not a constant, the overall efficiency of the recall is decreased and the output pulse is distorted depending on the specific function $\psi(\boldsymbol{r})$.

Appendix E: Estimation of noise from AFC with ACSS controlled readout

In this section the following assumptions are made:

1. $\Delta_{ac} \gg \Omega \rightarrow$ This allows the ACSS to be approximated by:

$$\frac{\Omega^2}{2\Delta_{ac}} \quad . \tag{E1}$$

2. $\Delta_{ac} \gg \Delta_{afc} \rightarrow$ This allows δt (the desired added delay due to the ACSS) to be approximated by:

$$\delta t \approx \frac{\Omega^2 \tau_{ac}}{{\Delta_{ac}}^2} = \frac{4\langle n \rangle g^2 \tau_{ac}}{{\Delta_{ac}}^2} \quad . \tag{E2}$$

The parameters for the AFC are as follows. Let the AFC have a characteristic width (FWHM) of Γ_{afc} that is greater than the Fourier bandwidth of a single photon that is to be stored. For simplicity, assume that the single photon envelope in time is a Gaussian with FWHM t_{sig}. We also assume that we have created a spectral filter that is only transmissive for the bandwidth of the stored pulse ($\Gamma_{sig} \approx 0.4413/t_{sig}$). Using this filter guarantees that all off-resonant photons excited by the ACSS pulses (Rabi frequency Ω, detuning of $\pm\Delta_{ac}$, and length τ_{ac}) are prevented from reaching the detector.

The excitation probability for a single ion in Γ_{sig} for a single ACSS pulse can be estimated by using the Lorentzian approximation for off-resonant excitation

$$\Pr(\text{ex}) \approx \frac{\Omega^2}{{\Delta_{ac}}^2 + \Omega^2} \quad . \tag{E3}$$

If we apply approximation (2) then we have that Eqn. E3 can be expressed

$$\Pr(\text{ex}) \approx \frac{\delta t}{\tau_{ac} + \delta t} \quad . \tag{E4}$$

Let the number of ions in Γ_{sig} be N (this includes ions in the teeth as well as the background). Therefore, the number of excited ions N_{ex} due to the two symmetrically applied ACSS pulses is approximately

$$N_{ex} \approx 2N \frac{\delta t}{\tau_{ac} + \delta t} \quad . \tag{E5}$$

Assume that all ions will emit radiatively into the cavity mode. Thus, the total number of noise photons is equal to N_{ex}. Some of these noise photons will be delayed by the AFC and hence, time-separated from the signal emission. Given a memory efficiency of η, this number is simply ηN_{ex}. Thus, the number of spontaneously emitted noise photons is $(1-\eta)N_{ex}$.

Given an optical lifetime of ions coupled to the cavity T_1^{cav}, a cavity input coupling rate κ_{in}, and a total loss rate κ, an upper bound on the number of noise photons that are indistinguishable in frequency, time, and space from the signal emission is

$$M_{noise} \approx \frac{\kappa_{in}}{\kappa} \frac{t_{sig}}{T_1^{cav}} (1-\eta) 2N \frac{\delta t}{\tau_{ac} + \delta t} \quad . \tag{E6}$$

Therefore, to minimize the noise and hence, maximize the fidelity of the ACSS controlled AFC the memory efficiency η should approach unity, and the bandwidth should be made large such that $\delta t \ll T_1^{cav}$ is possible. Ultimately, the all-optically controlled AFC will perform with the best fidelity in situations where the desired time delay is short compared to the fixed storage time of the unperturbed comb $2\pi/\Delta_{afc}$.